Materials Today Communications 22 (2020) 100842

Contents lists available at ScienceDirect

Materials Today Communications

journal homepage: www.elsevier.com/locate/mtcomm

Numerical study of the role of mush permeability in the solidifying mushy zone under forced convection

Haijie Zhang, Menghuai Wu*, Yongjian Zheng, Andreas Ludwig, Abdellah Kharicha

Montanuniversitaet Leoben, Austria

ARTICLE INFO

Keywords:
Fluid flow
Permeability
Mushy zone
Macrosegregation
Rotating magnetic field

ABSTRACT

Permeability of the mushy zone during alloy solidification is an important modeling parameter for many phenomena which accompany solidification, such as the formation of macrosegregation, shrinkage porosity, hot tearing, *etc.* The current study incorporates a two-phase, volume-average based columnar solidification model to study the role of mush permeability in the solidifying mushy zone under forced convection conditions. A unidirectional solidification of Al-7.0 wt %Si alloy sample (cylindrical with a diameter of 8 mm), referring to the experiments of MICAST project [Ratke, et al., MICAST research report – Phase IV, ESA-MAP AO-99-031, 2013], is considered. The forced convection is applied with a rotating magnetic field (20 m T). The basic permeability law for the numerical model is derived from Carman-Kozeny, but it has been modified by an artificial factor for the parameter study. The modeling results show that (1) the thickness of the mushy zone decreases and (2) the global macrosegregation intensity increases monotonically with growing permeability. A special macrosegregation profile resembling a "Christmas tree", as typically observed experimentally, could also be numerically predicted. However, the formation of the "Christmas tree" segregation profile depends strongly on the permeability of the material. The formation mechanism of "Christmas tree" segregation can be analyzed according to the flow-solidification interaction in the mushy zone. A quantitative determination of the permeability, depending on the dendritic structure of the mushy zone, is beyond the scope of the current study, nevertheless it also includes a brief discussion (literature review) on this topic.

1. Introduction

The interaction between the melt flow and developing mushy zone during solidification is still an issue that is not yet completely understood, although it plays an important role in the formation of microstructures and many other associated phenomena like macrosegregation, shrinkage porosity, hot tearing, *etc.* [1–4]. To investigate this flow-solidification interaction, a series of unidirectional solidification experiments on the Al-Si alloy system in the framework of the project MICAST (Microstructure Formation in Casting of Technical Alloys under Diffusive and Magnetically Convection Condition, supported by Europe Space Agency) were performed on Earth and in space [4–7]. A central Si-segregation in the shape of "Christmas tree" forms as the induction of the rotating magnetic field (RMF) becomes more intense, [6,7]. This "Christmas tree" segregation is characterized by a distinct accumulation of solute element (Si) along the axis of the sample, accompanied by many side-arms. Hereafter we also refer to the "Christmas tree" segregation as a central segregation channel with side-arms. A tentative explanation to this phenomenon would be that the solute rejected from the mushy zone was captured by multiple traveling Taylor-Görtler (T-G) vortices and brought back to the mushy zone [6]. Noeppel et al. [8] studied the effects of both rotating and travelling magnetic fields on macrosegregation during directional solidification, and suggested that the side-arms of the "Christmas tree" might form at the junction of two meridional T-G vortices ahead of the mushy zone. Similar studies were conducted by Budenkova et al. [9], but they found that the origins of the "Christmas tree" side-arms seem to occur independently of the T-G vortices. This is because the formation frequency of T-G vortices differs from the formation frequency of the segregation side-arms.

One parameter used to characterize the fluid flow in the mushy zone is permeability, which is normally described as a function of the liquid volume fraction and dendritic morphology of crystals in the mush (λ_1 and/or λ_2) [10–12]. The role of mush permeability in the formation of meso- or macro-segregation under natural convection conditions was studied as follows: the experimentally-reported macrosegregation pattern could only be modelled when a proper mush permeability law is implemented [13]; the formation of meso-segregation seems more

* Corresponding author at: Department of Metallurgy, Montanuniversitaet Leoben, Franz-Josef Street 18, A-8700, Leoben, Austria.
E-mail address: menghuai.wu@unileoben.ac.at (M. Wu).

https://doi.org/10.1016/j.mtcomm.2019.100842
Received 11 October 2019; Received in revised form 11 December 2019; Accepted 11 December 2019
Available online 19 December 2019

sensitive to the mush permeability than the formation of macrosegregation [14]. However, the influence of mush permeability on the mushy zone itself (*e.g.* mushy zone thickness), especially under forced convection conditions, is not yet sufficiently understood.

This paper presents a two-phase volume-average based solidification model, developed by Wu et al. [15–18], to simulate the unidirectional solidification of the binary Al-7.0 wt.%Si alloy under the conditions of RMF and nature convection. The main goal is to investigate the role of permeability in the formation of dendritic mushy zone (thickness) and macrosegregation. The formation mechanism of the "Christmas tree" segregation is analyzed in detail.

2. Numerical model and simulation settings

The two-phase volume-average based solidification model has already been described elsewhere [15–18]. The main features of the model and some assumptions are outlined below.

(1) The two phases refer to the liquid melt and columnar dendrite trunks as a solid phase. Both the liquid and solid phases are quantified by their volume fractions.
(2) The morphology of the columnar trunks is approximated as stepwise cylinders, growing unidirectionally along temperature gradient. The primary dendrites' arm spacing, λ_1, taken from the as-solidified structure, is assumed to be constant during solidification. The columnar tip front is traced according to LGK model [19].
(3) The net mass transfer rate from liquid to solid due to solidification is calculated according to the lateral growth speed of the columnar trunks, which is governed by the solute diffusion in the interdendritic melt around the columnar trunks.
(4) Volume-averaged concentrations of both liquid and solid phases are calculated. Macrosegregation is characterized by the mixture concentration among the liquid and solid. A thermodynamic equilibrium is assumed at the solid-liquid interface to determine the interfacial concentration. The concentration difference between the liquid thermodynamic equilibrium at the solid-liquid interface and the volume-averaged concentration in the interdendritic liquid is the driving force for the growth of columnar trunks. Back diffusion in the solid phase is not considered for the purpose of this study.
(5) A linearized binary Al-Si phase diagram with a constant liquidus slope and solute partition coefficient is considered.
(6) Fluid flow resistance through the mushy zone is calculated by means of a permeability law, referring to the Carman-Kozeny approach. For the purpose of conducting a numerical parameter study, it arbitrarily increases/decreases by orders of magnitude.
(7) Solidification shrinkage is not considered, and thermo-solutal convection is modelled with the Boussinesq approach.

The configuration of the sample is shown in Fig. 1. The cylindrical geometry, the alloy (Al-7.0 wt % Si) and the cooling conditions are taken from published work [9,20]. The alloy sample solidifies in an Al_2O_3 crucible directionally. The initial concentration (c_0) is set to be homogeneous in the sample. The initial temperature (T_0) of the liquid is set at 1190 K. On the top and bottom of the sample, a decreasing temperature is imposed T_{Top} and T_{Bottom}. As demonstrated in Fig. 1, before t = 100 s, T_{Top} is equal to T_{Bottom}. After t = 100 s, the temperature at the bottom (T_{Bottom}) begins to decrease. At t = 150 s the initial temperature gradient ($\vec{G}$) is generated. Then both T_{Top} and T_{Bottom} drop at the same cooling rate R, and the solidification subsequently occurs. The lateral wall of the sample is considered to be adiabatic. The mushy zone thickness (δ) is calculated as the distance from the solidification front to the point of eutectic temperature isotherm. An RMF inductor is installed outside the sample, which is controlled by a switch (on/off). The rotating magnetic field with a constant rotating frequency (f) and magnetic induction (B) is applied. The RMF is activated at the beginning of the calculation (t = 0 s) in the cases of chapter 3.1 and chapter 3.3, while the RMF is switched on at t = 650 s in the case of chapter 3.2. An analytical approximation of the azimuthal component of the electromagnetic force ($\vec{F}_\theta$) is valid (Eq. (1)) [6,21,22].

$$\vec{F}_\theta = \frac{1}{2}\sigma\omega B^2 r\left(1 - \frac{u_\theta}{\omega R}\right)\vec{e} \tag{1}$$

where σ is the electrical conductivity of the melt, $\omega = 2\pi f$ is angular frequency, B is the magnetic induction, r and R (= $d/2$) is a radial coordinate and radius of the sample, and u_θ is the azimuthal velocity magnitude of the melt at a radial coordinate r, $\vec{e}$ is the tangential unit vector. The material properties and other parameters used in the study are summarized in Table 1.

Two laws of the isotropic permeability (K) of the mushy zone, derived from the Carman-Kozeny law, are deployed: one as reported by Noeppel [8] referring to the secondary dendrite arm space λ_2; one as reported by Ramirez [24] referring to the primary dendrite arm space λ_1.

$$K = \frac{\lambda_2^2 f_\ell^3}{4\pi^2 K_c (1 - f_\ell)^2} \tag{2}$$

$$K = \frac{\lambda_1^2 f_\ell^3}{1667(1 - f_\ell)^2} \tag{3}$$

where K_c is a constant (K_c = 5), f_ℓ is the liquid volume fraction.

For the purpose of a numerical parameter study, five simulation cases are defined in Table 2. We take the permeability as reported by Ramirez as a reference case (K), three further cases are considered, for which the permeability is increased/decreased arbitrarily by a factor, *i.e.* 10 K, 0.1 K and 0.01 K.

The model is implemented in ANSYS FLUENT version 14.5, which uses a control-volume finite difference numerical method. All phases share a single pressure field, p, which is solved via a pressure correction equation. This, in turn is obtained from the sum of the normalized mass continuity equations, using the phase-coupled SIMPLE (PC-SIMPLE) algorithm. For each time step, 30 iterations are adopted to decrease the normalized residuals of concentration, flow quantities and continuity below 10^{-4} and enthalpy quantities below 10^{-7}. The decision to select a time step that ensures a high accuracy solution must be determined empirically by test simulations. In this study all calculations are run with a time-step of 0.0005 s. Parameter studies were performed in 2D axisymmetric (swirl) calculation; but full 3D simulations were made to verify the validity of 2D axisymmetric simulations for the flow (Chapter 3.1) and to analyze the solidification sequence (Chapter 3.2). The maximum mesh sizes are 3.0×10^{-4} m (3D) and 1.0×10^{-4} m (2D), respectively. One 3D simulation takes ca. 4 weeks; while one 2D simulation takes only a week on a high performance cluster (2.6 GHz, 12 cores).

3. Simulation results

3.1. Fluid flow

Fig. 2 shows the melt flow pattern in the sample at t = 80 s. The RMF is activated at the beginning of the calculation (t = 0 s). Under the RMF (20 m T, 50 Hz), an intensive azimuthal flow up to the velocity magnitude of 0.15 m/s is generated in the region at the center of the radius. Due to the non-slip flow boundary conditions at the lateral and bottom walls, a so-called Ekman effect [25] leads to a meridional circulation. The meridional velocity is 0.04 m/s, one order of magnitude smaller than the azimuthal velocity. As clearly demonstrated by the streamline in Fig. 2(b), the fluid rotates downwards at the periphery of the sample, then it rotates and flows upwards in the sample's center. What is more interesting to see is that the fluid flow is very unstable, as depicted in Fig. 2(a) and (c). The meridional velocity is characterized

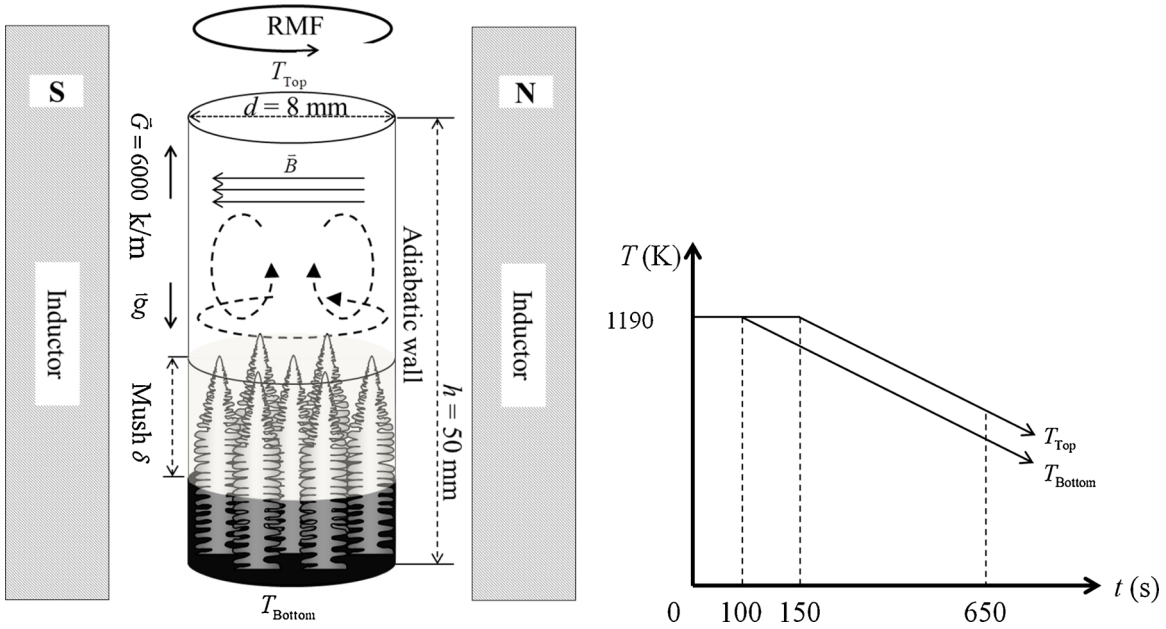

Fig. 1. Geometry configuration and boundary conditions.

Table 1
Summary of material properties and other parameters [8,23].

Property	Symbol	Units	Values
Thermophysical properties			
Specific heat	C_p^l C_p^s	J·Kg^{-1}·K^{-1}	1140.0
Latent heat	Δh_f	J·Kg^{-1}	400000.0
Diffusion coefficient (solid)	D_c	m^2·s^{-1}	1.0×10^{-12}
Diffusion coefficient (liquid)	D_ℓ	m^2·s^{-1}	6.45×10^{-9}
Thermal conductivity	k_p^l k_p^s	W·m^{-1}·K^{-1}	100.0
Liquid thermal expansion coefficient	β_T	K^{-1}	-1.85×10^{-4}
Liquid solutal expansion coefficient	β_c	wt.% $^{-1}$	1.3×10^{-3}
Reference density (solid)	ρ_{ref}	Kg·m^{-3}	2535.0
Boussinesq density difference	$\Delta\rho$	Kg·m^{-3}	165.0
Viscosity	μ_ℓ	Kg·m^{-1}·s^{-1}	2.52×10^{-3}
Electrical conductivity	σ	Ω^{-1}m^{-1}	3.65×10^6
Thermodynamic parameters			
Eutectic composition	c_{eu}	wt.%	12.6
Eutectic temperature	T_{eu}	K	850.0
Liquidus slope	m	K (wt. %)$^{-1}$	−6.62
Equilibrium partition coefficient	k	–	0.13
Primary dendritic arm spacing	λ_1	μm	300.0
Secondary arm spacing	λ_2	μm	50.0
Gibbs Thomson coefficient	Γ	m·K	2.41×10^{-7}
Melting point of solvent	T_f	K	933.5
Other parameters			
Initial concentration	c_0	wt.%	7.0
Initial temperature	T_0	K	1190.0
Cooling rate of top and bottom	R	K/s	0.16
Temperature gradient	$\vec{G}$	K/m	6000.0
Magnetic induction	B	mT	20.0
Angular frequency	ω	rad/s	314.0
Rotating frequency	f	Hz	50.0

by a random occurrence of Taylor-Görtler (T-G) vortices along the lateral wall of the sample [25]. Some T-G vortices move up and down to the top/bottom surface, and then disappear; while some of the vortices aggregate with the neighboring ones to form a large vortex. The generation and aggregation of these vortices seem to appear randomly. The space between every two vortices is about 5 mm. Note that this kind of flow pattern remains during solidification, interacting with the growing mushy zone.

Table 2
Cases definition for parameter study by varying permeability.

Cases	Expression	Relationship	Referred to	Parameters
A	–	0.01 K	–	$\lambda_1 = 300\mu m$ and $\lambda_2 = 50\mu m$, which are taken from experiments [4].
B	–	0.1 K		
C	$K = \frac{\lambda_1^2 f_\ell^3}{1667(1-f_\ell)^2}$	K	Ramirez [24]	
D	$K = \frac{\lambda_2^2 f_\ell^3}{4\pi^2 K_c (1-f_\ell)^2}$	4K	Noeppel [8]	
E	–	10K	–	

As a comparison to the 3D model, a 2D axisymmetric (swirl) calculation is performed, as depicted in Fig. 2(d). It is clear that the 2D axisymmetric calculation can successfully reproduce the 3D calculation results, in terms of both the velocity magnitude (azimuthal ~ 0.15 m/s, meridional ~ 0.04 m/s) and the flow pattern (*e.g.* T-G vortices). Even the spacing of each T-G vortex is also quite similar to that of the full 3D calculation. It can be concluded that the subsequent parameter study for the solidification based on 2D axisymmetric calculations is able to reproduce the key features of solidification as performed in full 3D. Two minor differences between 2D axisymmetric and 3D calculations should be kept in mind for the purpose of interpreting the solidification results from 2D calculations. One is that the instability of the flow, especially in the center region, is understated by the 2D axisymmetric calculation: the oscillation of the flow pattern in the center (3D) is smeared (averaged) when applying the 2D calculation. Another point is that the ideal axisymmetry of the result rendered in 2D would never occur in the full 3D calculation.

3.2. Solidification under RMF

The solidification process of the sample at t = 945 s under the influence of RMF is shown in Fig. 3. The RMF is activated at t = 650 s. The top and bottom boundaries of the mushy zone are represented by iso-surfaces of the liquid phase fraction (f_ℓ = 0.85) and eutectic temperature (T = 850 K), respectively. The distribution of the liquid phase fraction in the mushy zone, overlaid with the vectors of the liquid velocity is depicted in Fig. 3(a). The vector length is scaled by a log function. A tube-like channel, filled with solute-enriched liquid, forms in the sample center. It penetrates the entire mushy zone. In the mushy

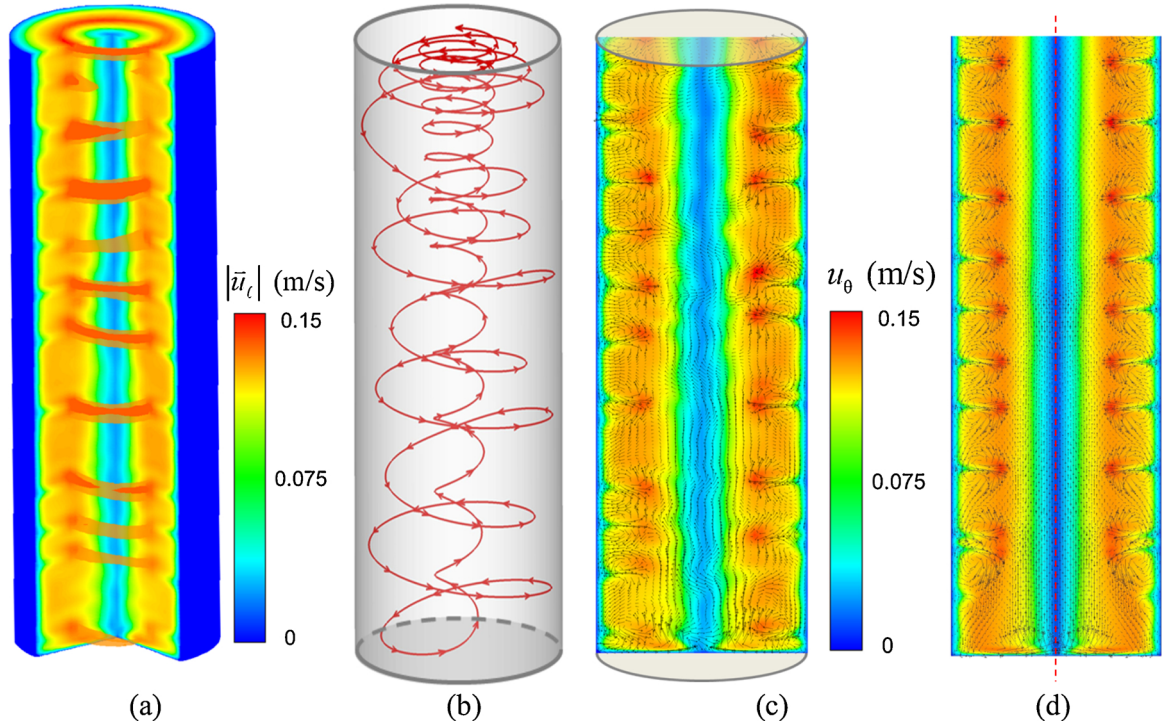

Fig. 2. Flow pattern of pure liquid melt under RMF (20 m T, 50 Hz) at the moment of 80 s before solidification starts: (a)–(c) in full 3D calculation, (d) in axisymmetric calculation. The domain is down-scaled in axis direction to allow a better view of the entire domain of the sample (φ 8 mm × 50 mm). (a) Contours of velocity magnitude (color scaled) in two vertical sections and one horizontal section at the top boundary, combined with two tube-like iso-surfaces of the velocity magnitude, which is used to indicate the typical Tayler-Görtler vortices [25]: one iso-surface is for the velocity magnitude of 0.135 m/s, one iso-surface, which is made transparent, is for the velocity magnitude of 0.13 m/s; (b) One streamline to show the mass transfer; (c) Contour of the azimuthal velocity (color scaled) in the central section, overlaid with the vectors of the meridional velocity in the central section; (d) Same contours/vector as in (c) in a 2D axisymmetric calculation (one half section is mirrored from another).

zone, the fluid flow is suppressed by the dendrites to a magnitude of $10^{-3}\sim10^{-6}$ m/s, and the maximum liquid velocity is observed in the tube-like channel. The flow pattern in the mushy zone is similar to that in the bulk liquid, as demonstrated in Chapter 3.1. The fluid rotates downwards at the periphery of the sample, then it rotates and flows upwards into the center tube-like channel – as demonstrated by the vectors in Fig. 3(a) and streamlines in Fig. 3(b). The central tube-like channel acts as a pump, sucking solute-enriched melt out of the mush and transporting it back into the bulk region of the sample.

As shown in Fig. 3(c)–(e), there is almost no macrosegregation in the lower part of the sample before the RMF is activated (before 650 s). The central segregation channel occurs only after the RMF stirring. The aforementioned T-G vortices still remain during solidification. With the gradual enrichment of the solute in the bulk melt region, the liquidus temperature decreases to about 873 K at 945 s. Fig. 3(d) shows the solute mixture concentration (c_{mix}). A strong positive macrosegregation channel, accompanied by side-arms, appears along the axis of the sample forms and it assumes the appearance of a “Christmas tree”. Liquid and columnar phase fractions are shown in Fig. 3(e) and (f). The distribution pattern of the liquid phase fraction (f_ℓ) is similar to that of c_{mix}. When the temperature is lower than eutectic temperature (T_{eu}), the remaining solute-enriched inter-dendritic liquid solidifies eutectically.

3.3. Role of the permeability in solidification

The calculation results of the solidification (620 s) by varying degrees of permeability are shown in Fig. 4. These five cases correspond to those in Table 2, which only lists the results in the mushy zone. In all cases, a central segregation channel with a diameter of 1 mm, strongly enriched with Si forms, where c_{mix} is close to the eutectic concentration. At the periphery of the sample, c_{mix} decreases with the rate of permeability. The degree of macrosegregation increases with the permeability. Except for the cases (a) and (e), all simulations present a “Christmas tree” segregation pattern. A characteristic time for the periodical formation of channels is relatively long (40 ~ 110 s).

Near the solidification front, the liquid velocity is close to that in the bulk liquid. In the deep mushy zone, the liquid velocity is decelerated by the resistance of the columnar dendrites, and the component of meridional liquid velocity ($\sim10^{-5}$ m/s) is several orders of magnitude smaller than that in the bulk liquid ($\sim10^{-2}$ m/s). As demonstrated by the pink dash lines in Fig. 4, as soon as side-arms of the segregation channel forms, the flow takes the path of the least resistance through the side-arms of the channel, hence the flow directions are strongly influenced by the forming side-arms. It is difficult to determine the maximum or average liquid velocity in the mushy zone, but it is still evident that the meridional liquid velocity increases with the rate of permeability. The mushy zone thickness (δ) is calculated from the distance between the solidification front and the eutectic isotherm. Clearly, δ decreases with the permeability.

4. Discussion

4.1. Relationship between the T-G vortex and segregation channel formation

As shown in Figs. 2 and 3, some T-G vortices form in the bulk liquid and move up/down to the top/bottom surface, and then disappear; while some of the vortices aggregate with the neighboring ones to form a big vortex. Taking the simulation case in Chapter 3.2 as a reference point, we measure the life time (formation interval) of each T-G vortex, which is compared with the time interval of formation of each side-arm of segregation channel. It is clear that the formation frequency of the side-arm is inverse proportional to its formation interval. The results

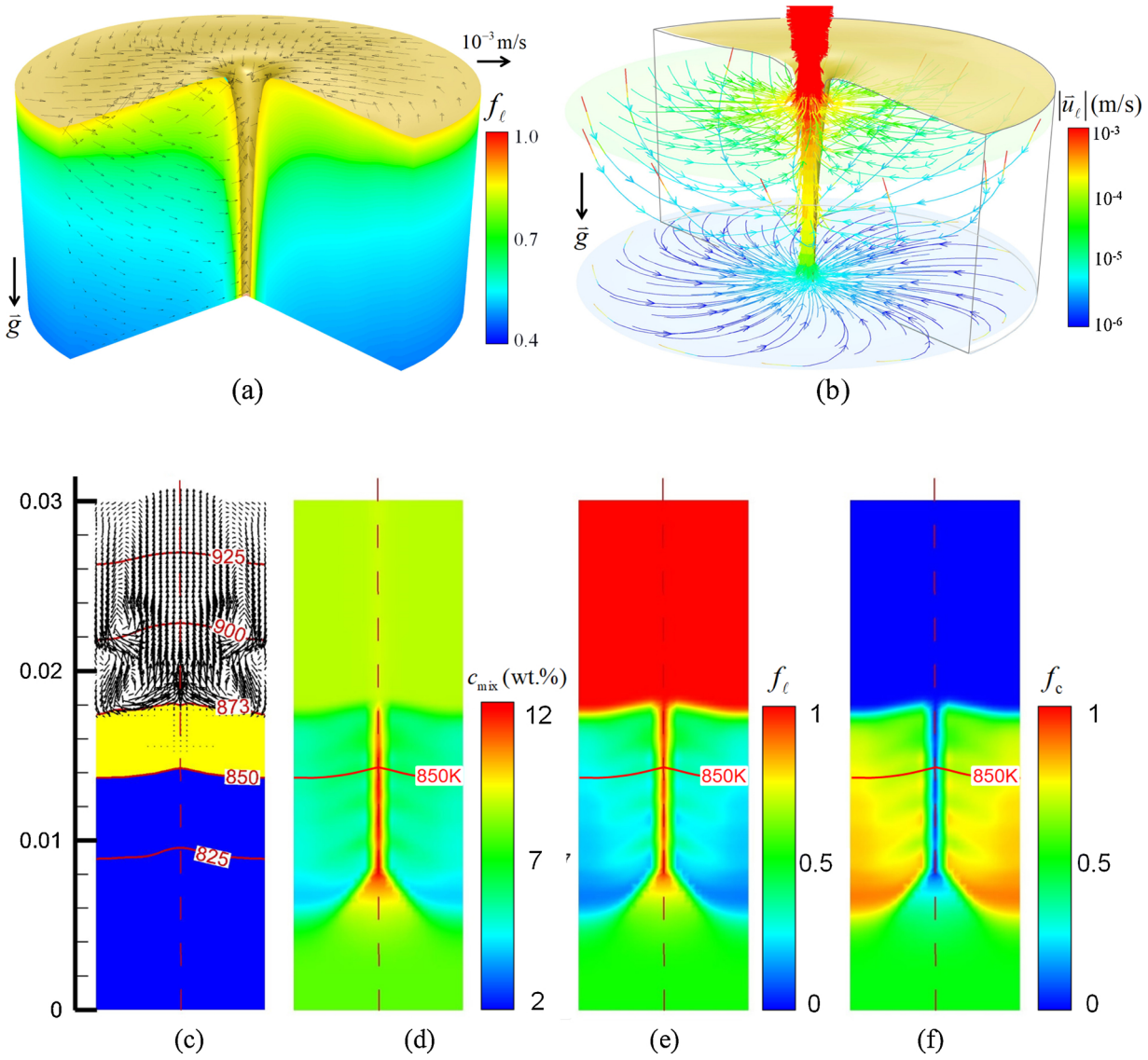

Fig. 3. The solidification process of the sample at the moment of 945 s: (a) and (b) in the mushy zone (3D), (c)–(f) in the whole domain (2D). (a) Contour of the liquid phase fraction (color scaled) in the mushy zone in two vertical sections and one iso-surface of the liquid phase fraction (f_ℓ = 0.85) at the top and center of the mush, overlaid with the vectors of the liquid velocity; (b) streamlines of the flow in the mushy zone colored by liquid velocity magnitude ($|\vec{u}_\ell|$); (c) different phase regions: bulk liquid by white, full solid by blue and the mushy zone by yellow, overlaid by isotherms and vectors of the meridional liquid velocity; (d) – (f) contours of mixture concentration (c_{mix}), liquid phase fraction (f_ℓ), and columnar phase fraction (f_c).

are plotted in Fig. 5. If one T-G vortex disappears at the solidification front, we record the time it takes for the melt to solidify. The interval of T-G vortex formation is calculated by the time difference between two subsequent records. Similarly, if one side segregation channel forms, we make a record of the solidification time. The formation interval of each segregation side-arm is calculated by the time difference between the two recorded time intervals.

As shown in Fig. 5 (insert), the formation interval of T-G vortex varies randomly between 0.3 and 1.2 s. On average, one T-G vortex disappears every 0.7 s at the solidification front. As the RMF is switched on at t = 650 s in this case, the first side channel forms at t = 680 s. The solute is gradually enriched in the bulk liquid due to the meridional liquid velocity. The enrichment of solute in the bulk liquid influences the solidification process. One influence is the increase of the formation interval of segregation side-arms. This interval changes from 40 to 110 s. A similar phenomenon was observed experimentally [26]. In the process of forming one side-arm, dozens of vortices form. The origin of the side-arms of the "Christmas tree" seems independent from the T-G vortices, supporting the conclusion of Bodenkova et al. [6], because the formation frequency of T-G vortices is approximately two orders of magnitude larger than the formation frequency of the side-arms of the "Christmas tree".

4.2. Role of permeability in mushy zone thickness and macrosegregation

The interaction between the melt flow and the formation of mushy zone is highly complex [27,28]. The fluid flow may influence the mushy zone by modifying the dendrite morphology: inducing the macrosegregation; causing segmentation and fragmentation. In turn, the mushy zone can affect the fluid flow by changing the flow intensity and pattern [28]. One parameter used to characterize the fluid flow in the mushy zone is permeability, *i.e.* a tensor to measure the ease of fluid flow through the solid network [12].

This article cannot cover all of the aforementioned aspects of the flow-solidification interaction, as it would go beyond the scope of an individual scientific paper. One of the most important objectives of this study is to demonstrate the influence of mush permeability on the solidification process by increasing or decreasing the permeability

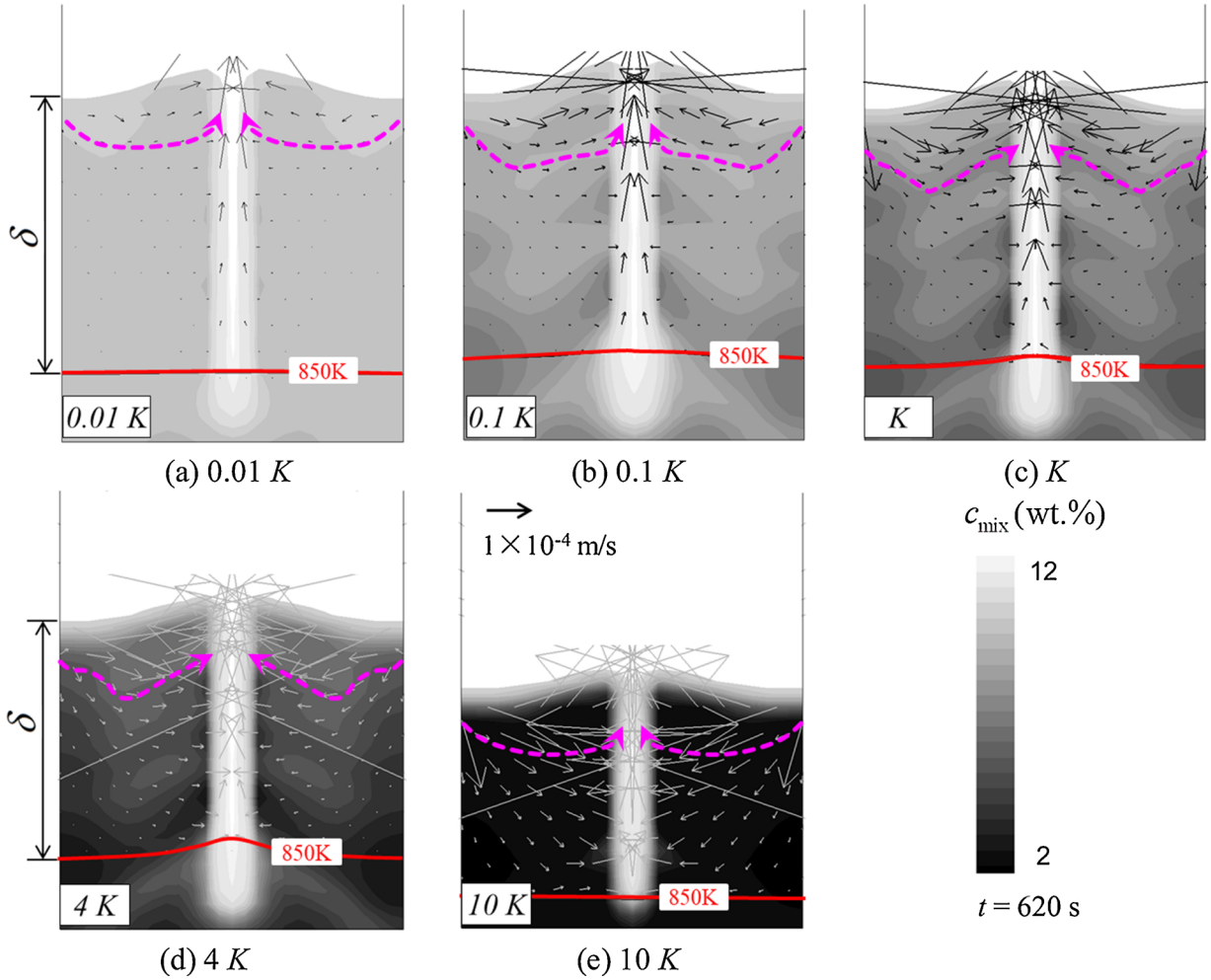

Fig. 4. Parameter study by varying rates of permeability. Cases (a)–(e), corresponding to those in Table 2, show the solidification in the mushy zone at 620 s. The gray-scale shows mixture concentration (c_{mix}) that is lighter for higher concentrations. Vector shows the meridional component of liquid velocity. The red solid lines are isotherms of the eutectic temperature, pink dash lines indicate the flow direction, and the top profile is the solidification front.

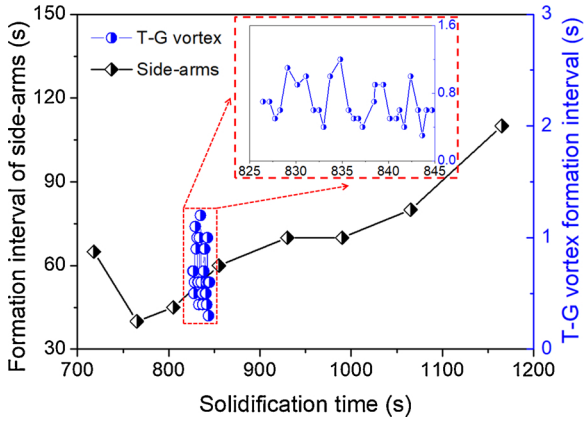

Fig. 5. Time intervals of the formation of T-G vortices and side-arms of central segregation channel.

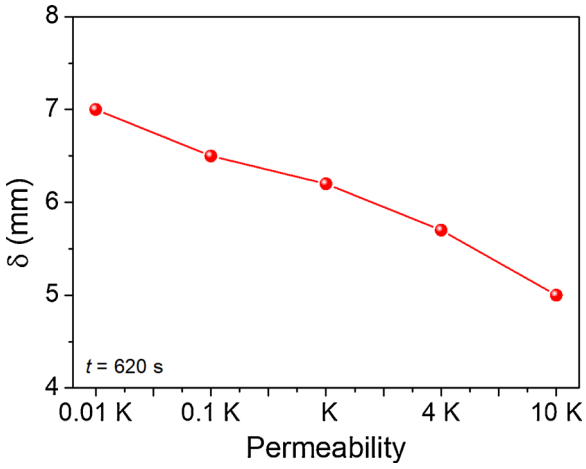

Fig. 6. Influence of permeability on mushy zone thickness (δ).

arbitrarily. This may help in understanding the effect of permeability on the flow-solidification interaction.

Based on the numerical simulation results, we have found that the thickness of mushy zone (δ) decreases with the permeability, and the macrosegregation severity increases, respectively. Quantitative analyses of the thickness of the mushy zone and mixture concentration have been performed. The mushy zone's thickness (δ) against the permeability is plotted in Fig. 6. Mushy zone thickness decreases from 7 mm to 5 mm when increasing the permeability by three orders of magnitude. The liquid velocity in the mushy zone is relatively rapid when there is a greater degree of permeability. The intense liquid velocity in the mushy zone promotes energy (enthalpy) and mass transport. This enhances the temperature gradient in/near the mushy zone.

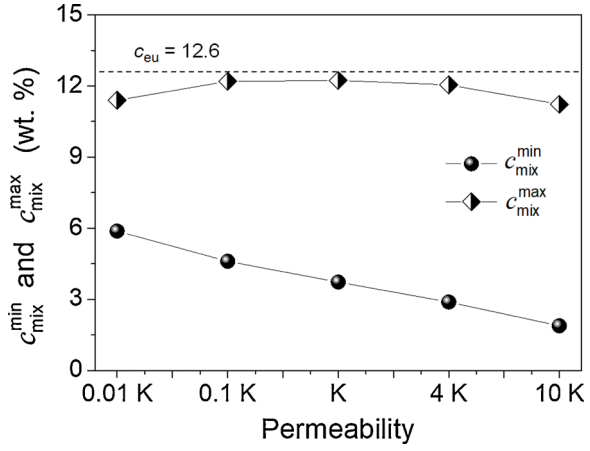

Fig. 7. Influence of permeability on macrosegregation.

The greater the temperature gradient, the thinner the mushy zone.

The minimum and maximum mixture concentrations (c_{mix}^{min}), (c_{mix}^{max}) against the permeability in the whole domain are plotted in Fig. 7. The hollow circles represent the maximum mixture concentration (c_{mix}^{max}), and the solid circles stand for the minimum mixture concentration (c_{mix}^{min}). The distance between these two lines indicates how heterogeneous the solute distribution actually is. This is consistent with the results shown in Fig. 4. The maximum mixture concentration (c_{mix}^{max}) of all these five cases, corresponding to the central positive segregation channel, is close to the eutectic concentration. The minimum mixture concentration, corresponding to negative segregation in the lower part of the periphery regions of the sample, decreases with the permeability. The more permeable the mush is, the stronger the flow, hence more solute will be transported from the periphery into the center and bulk regions of the sample.

Plenty of experiments and numerical simulations have been performed to determine the permeability of different alloys under varying casting conditions, and various permeability laws are therefore proposed [29–37]. The permeability was measured for different alloys [34,36,37]. Experimental methods fail to measure permeability when $f_\ell > 0.66$ in columnar structures, due to ripening and the fragile nature of dendrites. Recently, experimental 3D mapping of the sample using synchrotron X-ray micro-tomography followed by image analysis to distinguish the eutectic (interdendritic liquid) from the dendrite skeleton was used to reconstruct the dendritic morphology to generate 3D geometry [12,29–33], which makes the permeability calculations more accurate. However, the permeability values given by the different permeability formulas differ by two orders of magnitude. Extreme caution must be taken to in order to be able to precisely determine the permeability.

4.3. Side-arm formation of the central segregation channel

Reproducing the experimentally observed “Christmas tree” macrosegregation pattern works well by applying the current two-phase volume-average based solidification model. Li and Wu have proposed a formula to analyze the formation mechanism of channel segregation in the case of pure columnar solidification [16,17]. This formula is used to analyze the formation of the side-arms of the central segregation channel. The concentration difference between the liquid thermodynamic equilibrium at the solid-liquid interface and the volume-averaged concentration in the interdendritic liquid ($c_\ell^* - c_\ell$) is the driving force for both solidification and remelting. The local solidification/melting rate, $M_{\ell c}$, is proportional to $\frac{\partial(c_\ell^* - c_\ell)}{\partial t}$. The remelting of the dendrites is not considered in this work. The local solidification rate ($M_{\ell c}$) is the result of three contributions, corresponding to the three right hand side (RHS) terms of Eq. (4).

$$M_{\ell c} \propto \frac{\partial(c_\ell^* - c_\ell)}{\partial t} = \frac{(c_\ell - c_s^*)}{f_\ell}\frac{\partial f_\ell}{\partial t} + \frac{1}{m}\frac{\partial T}{\partial t} + \vec{u}_\ell \cdot \nabla c_\ell \quad (4)$$

where f_ℓ is liquid volume fraction, c_ℓ is species concentration in the liquid phase, c_ℓ^* and c_s^* are thermodynamic equilibrium species concentrations at the liquid/solid interface, and m is the liquidus slope. The first RHS term is the solidification-induced solute enrichment of the interdendritic melt. This term is always negative for solidification. The second RHS term is the contribution of the cooling rate, which is always positive. The third RHS term is the flow-solidification interaction term, which can be positive or negative, depending on the interdendritic flow direction. Local solidification behavior strongly depends on the intensity of the flow-solidification interaction.

In a region where the melt flows ($\vec{u}_\ell$) in the same direction as the liquid concentration gradient (∇c_ℓ), the flow-solidification interaction term is positive. The local increase in flow velocity due to a flow perturbation accelerates solidification. As a consequence, the local permeability (K) becomes relatively smaller than that of its neighboring zones, which decelerates the interdendritic fluid flow. Hence, side-arms would not form. On the contrary, in regions where the melt flows in the opposite direction of the concentration gradient, the flow-solidification interaction term is negative. The local increase in flow velocity due to flow perturbation suppresses the solidification rate. This region with a relatively lower solid fraction has a greater degree of permeability. The interdendritic fluid flow becomes stronger and side-arms form.

As shown in Fig. 8(a), the vectors of liquid velocity and solute gradient are both plotted in green and black, respectively. When the angle between these two vectors is larger than 90°, the flow-solidification interaction term should be negative. The suppressed solidification zone, corresponding to negative $\vec{u}_\ell \cdot \nabla c$, is shown in Fig. 8(b). It is evident that the solidification rate ($M_{\ell c}$) is far lower than that of the neighboring cells at the solidification front and sample center, where the flow-solidification interaction term ($\vec{u}_\ell \cdot \nabla c$) is negative. The suppressed solidification rate possibly leads to the formation of the side-arms of the channel. As depicted in Figs. 4 and 8(c), once the side-arm forms, the solute-enriched inter-dendritic liquid takes the path of least resistance through these zones. The enrichment of the solute-enriched liquid in the side-arms suppresses the solidification and even causes them to remelt [16,17]. Formation of the side-arms is a self-reinforcing process until the temperature falls below the eutectic temperature. The final segregation pattern is shown in Fig. 8(d), and the side-arm enclosed within the blue outline is newly formed at 620 s.

The “Christmas tree” macrosegregation under RMF has been experimentally observed for different alloys [38–40]. When the magnetic induction is week, the solidified microstructure is dominated by columnar dendrites [41]. With the increase of the magnetic induction, some equiaxed crystals form in the sample center [42]. Under a strong RMF, fragmentation occurs, leading to a transition in the microstructure from columnar to equiaxed (CET) [38]. The critical magnetic induction for CET is dependent on the respective alloy-system and cooling conditions. Study of CET under RMF is beyond the scope of the current paper. Based on the published results, the solidified microstructure of the sample under current cooling conditions and RMF strength should be dominated by columnar dendrites [6,42].

5. Conclusion

A two-phase volume-average based columnar solidification model is used to calculate the unidirectional solidification process of a cylindrical sample (φ 8 mm × 50 mm, Al-7.0 wt.%Si alloy) under RMF (Rotating magnetic field, 20 m T, 50 Hz) with a focus on evaluating the effects of mush permeability on the solidifying mush zone. Following conclusions are drawn.

1) It is verified that the flow calculation under RMF in 2D axisymmetry (swirl) can sufficiently reproduce the full 3D calculation, in terms of

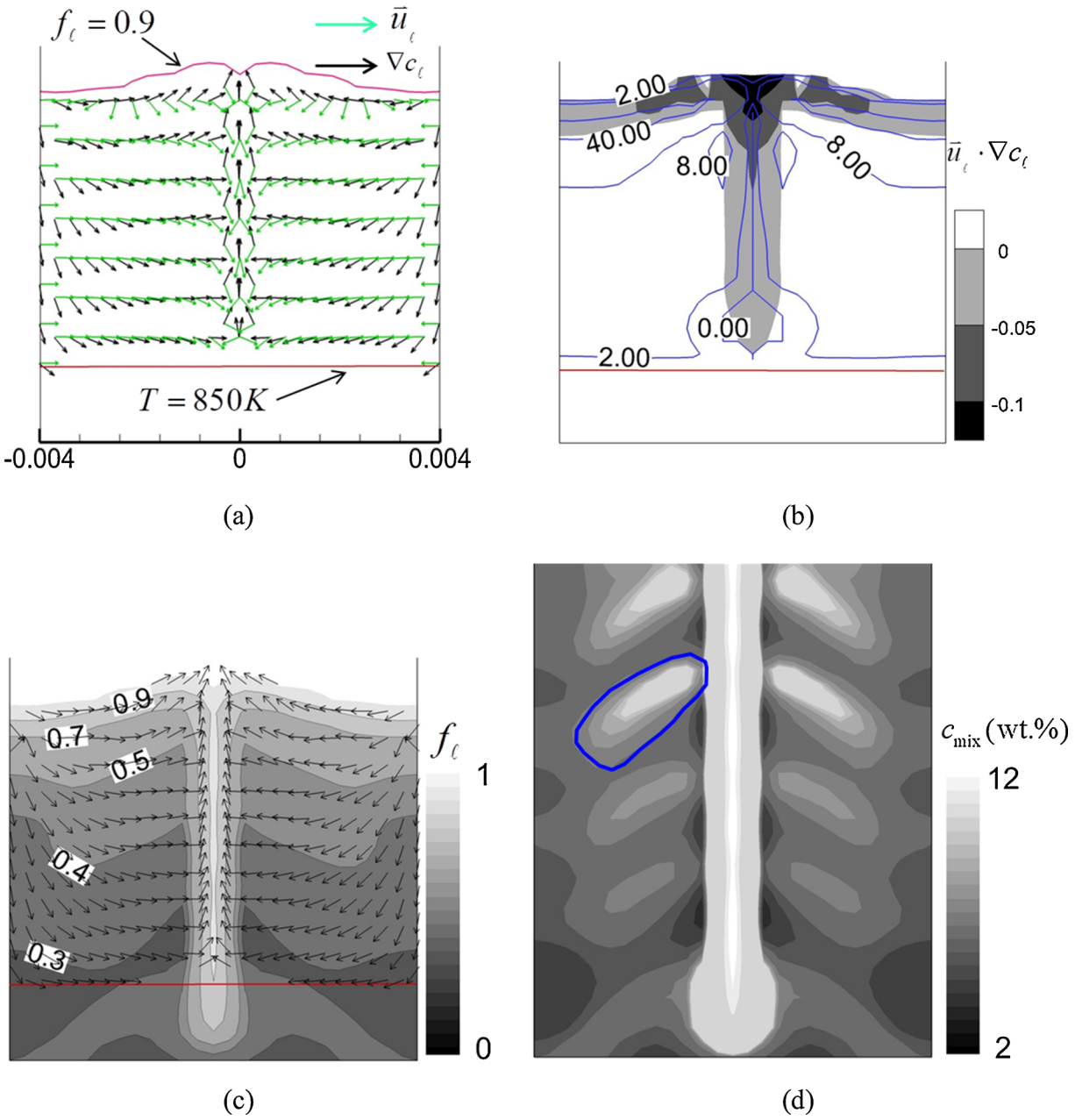

Fig. 8. Analysis of the formation of the side-arms in the central segregation channel at t = 620 s: (a) vector of liquid velocity (green) overlaid by vector of solute gradient; (b) contours of the flow-solidification interaction term ($\vec{u}_\ell \cdot \nabla c_\ell$) in white (positive value) and dark (negative value) overlaid by the solidification rate ($M_{\ell c}$) isolines; (c) liquid volume fraction (f_ℓ) contours and isolines overlaid by vectors of liquid velocity; and (d) final mixture concentration (c_{mix}).

both the velocity magnitude (azimuthal ~ 0.15 m/s, meridional ~ 0.04 m/s) and the flow pattern (*e.g.* T-G vortices). Mesh sizes of both 2D and 3D calculations must be rigorously controlled.

2) Numerical parameter study shows that the thickness of the mushy zone decreases and the global macrosegregation intensity increases monotonically with the mush permeability.
3) The "Christmas tree" macrosegregation pattern, sometimes observed experimentally, can only occur when the permeability falls in a certain range for the case of pure columnar solidification. Literature studies indicate that permeability rates, as suggested by different permeability laws, differ from by two orders of magnitude, hence extreme caution must be taken in order to correctly determine the permeability. The formation of side-arms of "Christmas tree" macrosegregation during solidification can be analyzed in accordance with the flow-solidification term ($\vec{u}_\ell \cdot \nabla c$).
4) The origin of the "Christmas tree" channels seems independent from the T-G vortices, supporting the conclusion of Bodenkova et al. [6], as the formation frequency of T-G vortices is approximately two orders of magnitude greater than the formation frequency of the "Christmas tree" channels.

CRediT authorship contribution statement

Haijie Zhang: Conceptualization, Methodology, Investigation, Writing - original draft, Visualization. **Menghuai Wu:** Conceptualization, Methodology, Writing - review & editing, Project administration. **Yongjian Zheng:** Conceptualization, Methodology. **Andreas Ludwig:** Conceptualization, Supervision. **Abdellah Kharicha:** Conceptualization, Software.

Declaration of Competing Interest

None.

Acknowledgements

The authors acknowledge the financial support from Austrian Research Promotion Agency (FFG) -Austrian Space Application Program (ASAP) through the project FLOWSICONS (No. 859777), as well as the support from European Space Agency (ESA) through the project MICAST.

References

[1] A.V. Reddy, N.C. Beckermann, Metall. Mater. Trans. B 28 (1997) 479–489.
[2] M. Rappaz, J.M. Drezet, M. Gremaud, Metall. Mater. Trans. A 30 (1999) 449–455.
[3] D.M. Stefanescu, Int. J. Cast Met. Res. 18 (2005) 129–143.
[4] Ratke, et al., MICAST Research Report – Phase IV, ESA-MAP AO-99-031 (2013).
[5] D.R. Liu, N. Mangelinck-Noël, C.A. Gandin, G. Zimmermann, L. Sturz, H.N. Thi, B. Billia, Acta Mater. 64 (2014) 253–265.
[6] O. Budenkova, A. Noeppel, J. Kovács, A. Rónaföldi, A. Roósz, A.M. Bianchi, F. Baltaretu, M. Medina, Y. Fautrelle, Mater. Sci. Forum. 649 (2010) 269–274.
[7] J. Kovács, A. Rónaföldi, A. Roósz, Mater. Sci. Forum. 649 (2010) 263–268.
[8] A. Noeppel, A. Ciobanas, X.D. Wang, K. Zaidat, N. Mangelinck, O. Budenkova, A. Weiss, G. Zimmermann, Y. Fautrelle, Metall. Mater. Trans. B 41 (2010) 193–208.
[9] O. Budenkova, F. Baltaretu, J. Kovács, A. Roósz, A. Rónaföldi, A.M. Bianchi, Y. Fautrelle, IOP Conf. Series: Mater. Sci. Eng. 33 (2012) 012046.
[10] D.R. Poirier, Metall. Mater. Trans. B 18 (1987) 245–255.
[11] M.C. Schneider, C. Beckermann, Int. J. Heat Mass Transf. 38 (1995) 3455–3473.
[12] C. Puncreobutr, A.B. Phillion, J.L. Fife, P.D. Lee, Acta Mater. 64 (2014) 316–325.
[13] A.K. Singh, B. Basu, A. Ghosh, Metall. Mater. Trans. B 37 (2006) 799–809.
[14] A. Kumar, M. Založnik, H. Combeau, Int. J. Therm. Sci. 54 (2012) 33–47.
[15] M. Wu, Y. Zheng, A. Kharicha, A. Ludwig, Comput. Mater. Sci. 124 (2016) 444–455.
[16] J. Li, M. Wu, J. Hao, A. Kharicha, A. Ludwig, Comput. Mater. Sci. 55 (2012) 419–429.
[17] J. Li, M. Wu, J. Hao, A. Ludwig, Comput. Mater. Sci. 55 (2012) 407–418.
[18] M. Wu, A. Ludwig, A. Kharicha, Appl. Math. Model. 41 (2017) 102–120.
[19] J. Lipton, M.E. Glicksman, W. Kurz, Mater. Sci. Eng. 65 (1984) 57–63.
[20] J. Kovács, A. Rónaföldi, A. Roósz, Trans. Indian Inst. Met. 62 (2009) 475–477.
[21] J.K. Roplekar, J.A. Dantzig, Int. J. Cast Met. Res. 14 (2001) 79–95.
[22] A. Noeppel, A. Ciobanas, X.D. Wang, K. Zaidat, N. Mangelinck, O. Budenkova, A. Weiss, G. Zimmermann, Y. Fautrelle, Metall. Mater. Trans. B 41 (2010) 193–208.
[23] M. Ghods, L. Johnson, M. Lauer, R.N. Grugel, S.N. Tewari, D.R. Poirier, J. Cryst. Growth 441 (2016) 107–116.
[24] J.C. Ramirez, C. Beckermann, Metall. Mater. Trans. A 34 (2003) 1525–1536.
[25] B. Willers, S. Eckert, P.A. Nikrityuk, D. Räbiger, J. Dong, K. Eckert, G. Gerbeth, Metall. Mater. Trans. B 39 (2008) 304–316.
[26] A. Roósz, J. Kovács, A. Rónaföldi, Á. Kovács, Mater. Sci. Forum. 752 (2013) 57–65.
[27] H. Wang, M.S. Hamed, S. Shankar, J. Mater. Sci. 53 (2018) 9771–9789.
[28] M. Wu, A. Vakhrushev, G. Nummer, C. Pfeiler, A. Kharicha, Open Transp. Phenom. J. 2 (2010) 16–23.
[29] D. Bernard, Ø. Nielsen, L. Salvo, P. Cloetens, Mater. Sci. Eng. A 392 (2005) 112–120.
[30] D. Fuloria, P.D. Lee, D. Bernard, Mater. Sci. Eng. A 494 (2008) 3–9.
[31] E. Khajeh, D.M. Maijer, Mater. Sci. Technol. 26 (2010) 1469–1476.
[32] E. Khajeh, D.M. Maijer, Acta Mater. 58 (2010) 6334–6344.
[33] E. Khajeh, D.M. Maijer, Acta Mater. 59 (2011) 4511–4524.
[34] N. Streat, F. Weinberg, Metall. Trans. B 7 (1976) 417–423.
[35] T. Takaki, S. Sakane, M. Ohno, Y. Shibuta, T. Aoki, Acta Mater. 164 (2019) 237–249.
[36] A.J. Duncan, Q. Han, S. Viswanathan, Metall. Mater. Trans. B 30 (1999) 745–750.
[37] D. Apelian, M.C. Flemings, R. Mehrabian, Metall. Trans. 5 (1974) 2533–2537.
[38] J. Kovács, A. Rónaföldi, Á. Kovács, A. Roósz, Trans. Indian Inst. Met. 62 (2009) 461–464.
[39] M. Svéda, A. Sycheva, J. Kovács, A. Rónaföldi, A. Roósz, Mater. Sci. Forum. 790–791 (2014) 414–419.
[40] J. Kovács, A. Rónaföldi, A. Roósz, Mater. Sci. Forum. 790–791 (2014) 408–413.
[41] S. Steinbach, L. Ratke, Mater. Sci. Eng. A 413–414 (2005) 200–204.
[42] G. Zimmermann, A. Weiss, Z. Mbaya, Mater. Sci. Eng. A 413 (2005) 236–242.